Commissioning of the new Beam Halo Monitoring system for the CMS experiment

A THESIS
SUBMITTED TO THE UNIVERSITY HONORS PROGRAM
OF THE UNIVERSITY OF MINNESOTA
BY

Kelly M. Stifter

IN PARTIAL FULFILLMENT OF THE REQUIREMENTS
FOR THE DEGREE OF
BACHELOR OF SCIENCE, SUMMA CUM LAUDE
IN PHYSICS

Under the supervision of Roger Rusack

August, 2015

Acknowledgements

First and foremost, I would like to thank my research advisor, Prof. Roger Rusack. Throughout my undergraduate career, he has been an unceasing source of opportunities, wisdom, and encouragement. I can not fully express my gratitude for his suggestion to spend a semester at CERN, and I am so very thankful for his confidence in me.

I would also like extend my gratitude to the rest of my thesis committee: Prof. Jeremy Mans and Dr. Anne Dabrowski. Their technical expertise and management experience served as the driving force for this experiment.

I would like to thank the University of Minnesota and the Department of Physics and Astronomy for making my semester at CERN possible, as well as CERN and BRIL for graciously taking me on as a student.

Finally, none of this research would have been possible if not for my two BHM colleagues: Nicolò Tosi and Stella Orfanelli. They answered my incessant questions, and from them I have learned a truly ridiculous amount.

Additional thanks go to all of the CERN, University of Minnesota, and University of Bologna students and technicians for all of their contributions to the project.

Abstract

A new Beam Halo Monitor (BHM) detector system has been installed in the CMS cavern to measure the machine-induced background (MIB) from the LHC. This background originates from interactions of the primary beam halo with the final set of collimators before the CMS experiment and from beam gas interactions. The BHM detector uses the directional nature of Cherenkov radiation and event timing to select particles coming from the direction of the beam and to suppress those originating from the interaction point. It consists of 40 quartz cylinders, placed on each side of the CMS detector, coupled to UV-sensitive PMTs. For each bunch crossing, the PMT signal is digitized by a charge integrating ASIC and the arrival time of the signal is recorded. The data are processed in real time to yield a precise measurement of per-bunch-crossing MIB rate for each beam. This measurement is made available to CMS and the LHC, in order to provide real-time feedback on the beam quality and improve the efficiency of data taking. The BHM detector is now in the commissioning phase, and first results have been obtained.

Contents

List of Figures

Chapter 1

Introduction

The Large Hadron Collider (LHC) is part of the large accelerator complex operated by CERN. In the LHC, two beams of protons are accelerated in opposite directions through a 27km circumference ring of superconducting magnets before being collided at four interaction points around the ring. At its design energy, the LHC collides protons with a center of mass energy of 14TeV. After two years of maintenance and upgrades during Long Shutdown 1 (LS1), the machine reached 13TeV, the highest energy so far, in June 2015. The LHC is now expected to deliver a luminosity of $2 \times 10^{34}\mathrm{cm}^{-2}\ \mathrm{s}^{-1}$ until 2025. A full description of the machine can be found in Ref. [2].

The Compact Muon Solenoid (CMS) experiment is a general purpose particle detector located at one of the four interaction points of the LHC. An overview of the detector can be seen in Fig. 1.1.

The central feature of the CMS apparatus is a superconducting solenoid of 6m internal diameter, providing a magnetic field of 3.8T. Within the superconducting solenoid volume are a silicon pixel and strip tracker used to reconstruct vertices and tracks, a lead tungstate electromagnetic calorimeter (ECAL) used to measure the energy of electrons and gammas, and a brass and scintillator hadron calorimeter (HCAL) used to measure the energy of hadrons. Muons are measured in gas-ionization detectors embedded in the steel flux-return yoke outside the solenoid. All detectors are composed of a barrel section and two endcap sections. Extensive forward calorimetry, including a forward hadron calorimeter (HF), complements the coverage provided by the barrel and endcap detectors. A detailed description of the CMS detector can be found in Ref. [3].

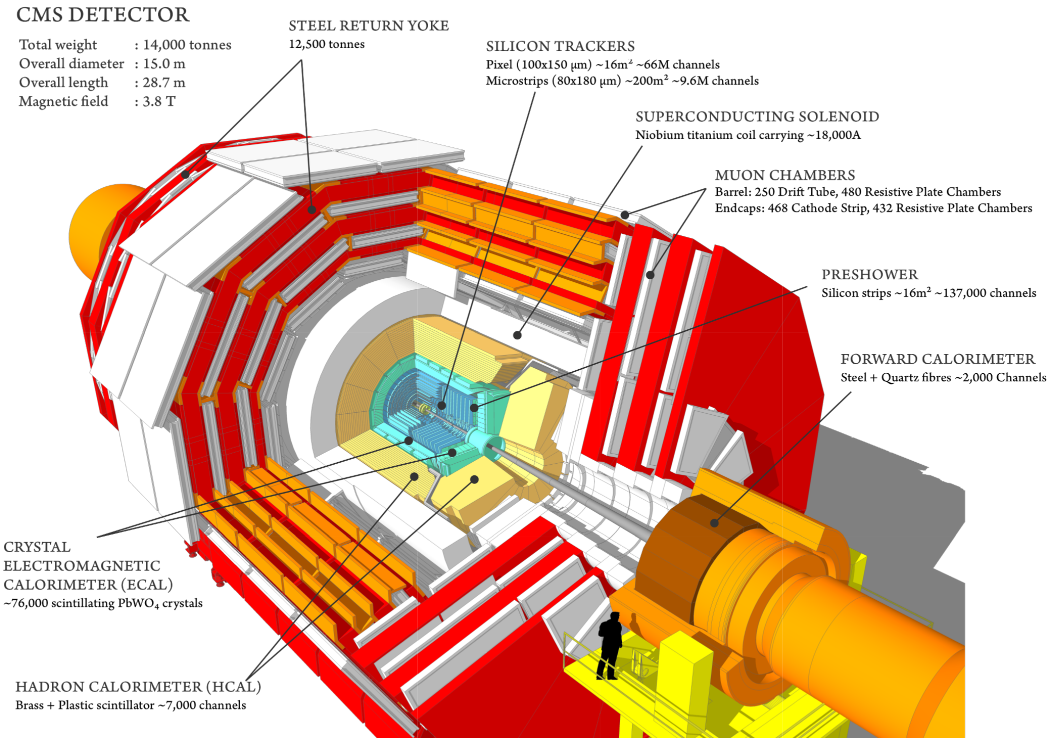

Figure 1.1: An overview of the CMS detector.

Together with the ATLAS experiment [4], the CMS collaboration announced the discovery of the Higgs Boson in July 2012 [5], [6]. Now, CMS will be looking for evidence of physics beyond the Standard Model of particle physics during Run II.

CMS is equipped with several detectors that measure luminosity and monitor beam backgrounds. During LS1, these efforts were consolidated, and the Beam, Radiation, Instrumentation, and Luminosity (BRIL) group was established. The primary goal of BRIL is developing, implementing, and operating a set of complementary subdetectors that monitor LHC beam conditions in order to provide feedback to the LHC and to ensure safe data-taking conditions for CMS. An overview of BRIL subdetectors can be seen in Fig. 1.2. Upgrades to a number of these systems were implemented during LS1 [7]. Further information on the various systems can be found in Ref. [8], [9], and [10]. Additional BRIL responsibilities include providing online luminosity measurements and simulating and measuring background radiation in the CMS cavern.

A new Beam Halo Monitor (BHM) has been developed by BRIL and was installed

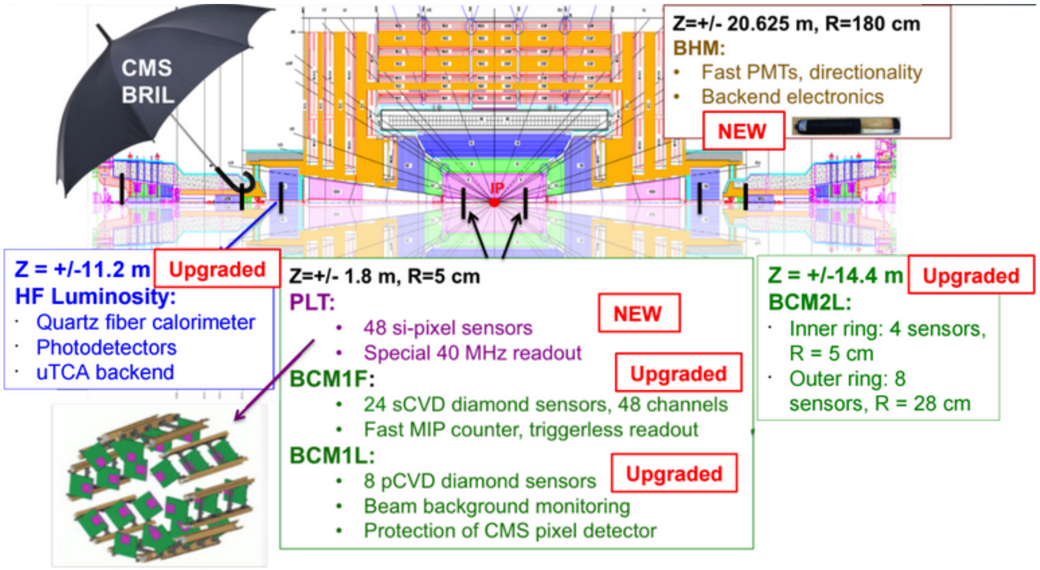

Figure 1.2: An overview of all BRIL subdetectors.

during LS1. It consists of forty detector units that rely on the directional nature of Cherenkov radiation in order to measure the machine-induced background (MIB) rate for each beam arriving at CMS at a large radius. The design, installation, and commissioning of the BHM detector are the main subjects of this report. These activities are the collaborative work of a number of physicists and engineers from several institutions, including CERN, University of Minnesota, University of Bologna, and National Technical University of Athens. For the purpose of this thesis, the author's contributions will be highlighted where relevant.

Chapter 2

Large Hadron Collider

The LHC [2] is the largest and most sophisticated tool being used to study the Standard Model of particle physics. In the LHC, two counter-rotating proton beams are accelerated up to 7TeV. Beam 1 travels in the clockwise direction, while beam 2 travels in the counterclockwise direction.

The machine is divided into eight arcs and eight straight sections. Each arc contains dipole bending magnets, and the straight sections have higher-order focusing magnets. In four of the straight sections, there are interaction points (IPs), or places at which the two beams are collided. The remaining four straight sections are not interaction points, and instead house utility insertions. The CMS experiment is located at point 5, opposite to the ATLAS experiment at point 1, as shown in Fig. 2.1.

At maximum capacity, each ring holds 2808 bunches of protons that collide at the four interaction points around the ring. A nominal bunch contains approximately 10^{11} protons. Each bunch is a few centimeters long, but varies widely in transverse dimensions as it travels through the LHC. While in the curved sections, it may be up to several millimeters in diameter. It is then focused down to approximately 16μm when nearing a collision point, in order to increase interaction probability. The focusing is performed by about 400 main quadrupole magnets, with many smaller magnets to provide minor corrections. The final focusing before a collision point is performed by a series of three quadrupole magnets, located on either side of the experimental caverns at points 1 and 5.

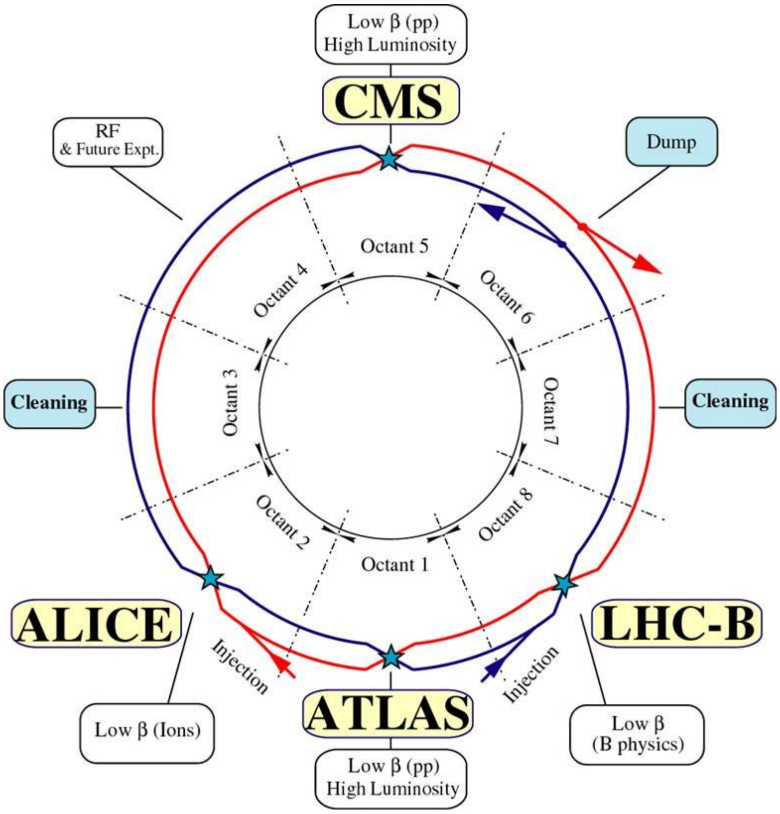

Figure 2.1: Layout of the LHC.

2.1 Machine-induced Background

Over time, protons can diffuse outward from their bunches in both the transverse and longitudinal directions. This is caused mainly by Coulomb scattering off residual gas in the vacuum of the beam pipe or interactions with other protons in the bunch [11]. These losses need to be controlled because a local transient loss of 4×10^7 protons can induce a quench in the superconducting magnets, causing the LHC to be off for several hours. In order to prevent this, the beams are ‘cleaned’ by a collimation system [12].

A collimator is a set of mechanical jaws that close around the beam. An image of an LHC collimator is shown in Fig. 2.2. The primary collimators in the LHC are 20cm long tungsten jaws that have a maximum aperture of 60mm and a minimum aperture of 0.5mm. As the jaws are moved closer together, particles in the periphery of the beam are absorbed or scattered.

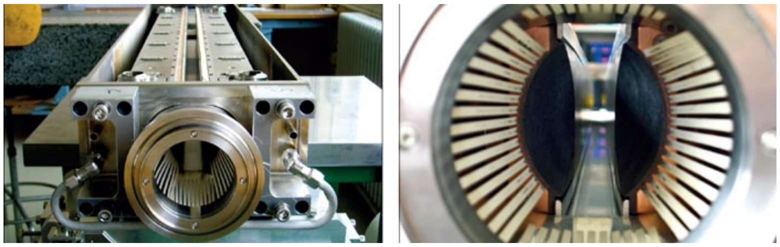

Figure 2.2: An LHC collimator.

The LHC has two main collimation systems. The system responsible for momentum cleaning is located at point 3, and the betatron cleaning system is housed in point 7. In both systems, particles with either a large transverse or longitudinal oscillation are scattered by the Target Collimator Primary (TCP). These interactions create a secondary halo. For this reason, the TCP is followed by the Target Collimator Secondary (TCS), which scatters the losses from interactions with the TCP, as well as any remaining primary beam halo. An additional Target Collimator Tertiary (TCT) is located on either side of points 1 and 5 in order to provide local protection for the quadrupole triplets. An overview of the collimation system is shown in Fig. 2.3.

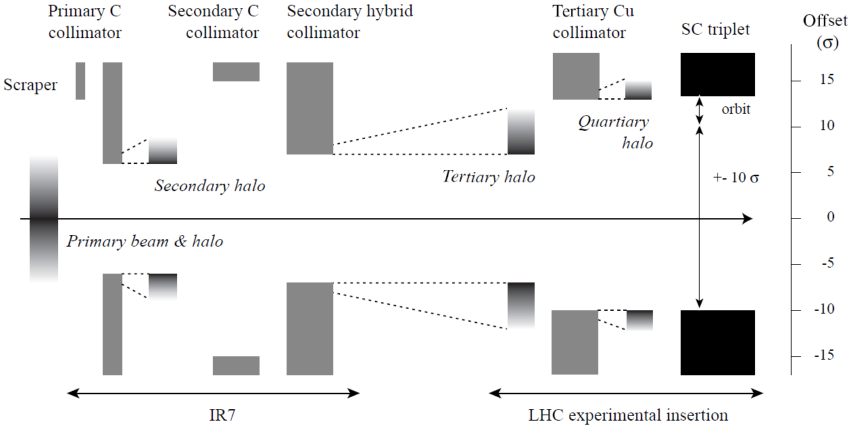

Figure 2.3: Collimation system for the LHC.

In addition to interactions with collimators, interactions with residual gas in the beam pipe also contribute to the beam halo. Events that occur far away from experimental areas can contribute to the beam halo if particles are deflected with a small scattering angle or suffer a small momentum loss, causing them to travel a long distance around the ring before exiting to the beam halo. Further beam gas interactions may occur downstream from the collimation systems.

After passing the final set of collimators, the remaining beam halo then propagates into the experimental caverns and is known as machine induced background (MIB). A major component of this background is high energy muons, because other particles quickly decay or get absorbed.

A MIB event in CMS is shown in Fig. 2.4. These particles are an unwanted background for the detectors. For example, they can leave large energy deposits in calorimeters, which interfere with the reconstruction of missing energy. In the case of CMS, this background is particularly troublesome for the Cathode Strip Chambers (CSCs) [13], which are muon detectors located on the endcaps. A high MIB rate significantly increases the false trigger rate of this portion of the detector, causing data-taking inefficiencies.

The BHM system was designed to monitor this background for CMS in real time to alert the LHC operations to possible beam instabilities.

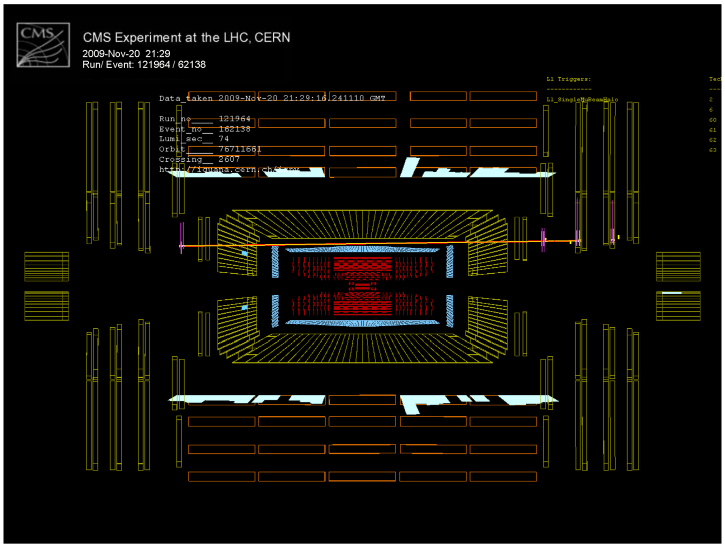

Figure 2.4: A machine-induced background event, as seen in the CMS detector.

Chapter 3

Detector Concept

The purpose of the new Beam Halo Monitor (BHM) is to provide an online, bunch-by-bunch MIB rate arriving at CMS at a high radius for both of the LHC beams.

A major difficulty in determining a background rate for incoming beam halo particles is separating them from outgoing collision products (PP) and particles from other background sources such as activated material or cosmic rays. As shown in Fig. 3.1, there is a factor of 10^3 more PP particles than MIB particles [1]. The challenge, then, is to separate these two types of events. The goal is the suppression of PP events by a factor of 10^3 in order to see a signal-to-noise ratio of 1. To achieve this, the BHM detector takes advantage of both the directionality and timing of the two types of particles.

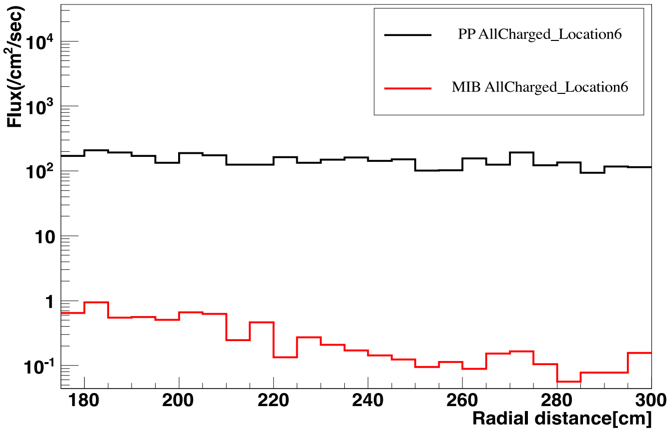

Figure 3.1: Absolute fluxes of MIB and PP particles at various radii. The BHM detector is located at 1.8 m. At this location, a factor of 10^3 separates the PP and MIB particles.

3.1 Cherenkov Radiation

One way to make use of directionality is through Cherenkov radiation [14], which is produced by a charged particle that travels faster than the speed of light in a material.

The speed of light in a material, v_{mat}, is affected by the index of refraction of the material, n, as shown in Eq. (3.1).

$$v_{mat} = c/n \tag{3.1}$$

Since the index of refraction is a number greater than one, the speed of light in any material is always less than the speed of light in a vacuum. Consequently, for a sufficiently high-energy particle, it is possible to exceed v_{mat}.

A charged particle traveling through a material at a constant speed creates an electromagnetic field which propagates at speed v_{mat}. This electric field accelerates the electrons in the material. If the particle is traveling at a speed less than v_{mat}, as in Fig. 3.2(a), then the energy imparted to the electrons simply dissipates through the material as heat. When the particle is traveling at or above v_{mat}, as in Fig. 3.2(b), its electromagnetic field interferes with itself constructively. The resulting shockwave manifests itself as coherent photons, called Cherenkov radiation. A full derivation of the phenomena is presented in Ref. [15], but the basic theory is outlined below.

By considering the geometry of the Cherenkov cone as shown in Fig. 3.3, the angle, θ_c, at which the photons are emitted relative to the moving particle, can be determined as a function of β, the ratio of the particle's speed to the speed of light in a vacuum, as shown in Eq. 3.2.

$$\cos\theta_c = \frac{1}{\beta n} \tag{3.2}$$

The minimum particle velocity that will produce Cherenkov radiation is v_{mat}, at which the Cherenkov angle is 0°. The Cherenkov angle reaches a maximum of $\cos^{-1}(\frac{1}{n})$ as the speed of the particle approaches c. Since there is a threshold velocity, there is a corresponding threshold energy that can be calculated by applying the threshold condition of $\beta = \frac{1}{n}$ to the equation for relativistic energy. The result is shown in Eq. 3.3.

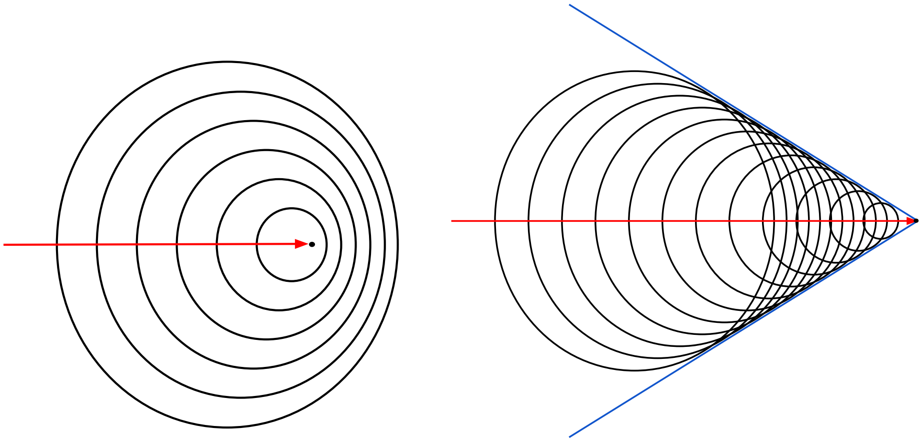

(a) No Cherenkov Radiation (b) Cherenkov Radiation

Figure 3.2: *Left:* A particles travels less than the speed of light through a material. There is no constructive interference, and Cherenkov radiation is not produced. *Right:* A particle travels faster than the speed of light through a material. Its electromagnetic field interferes constructively with itself, and Cherenkov radiation is produced.

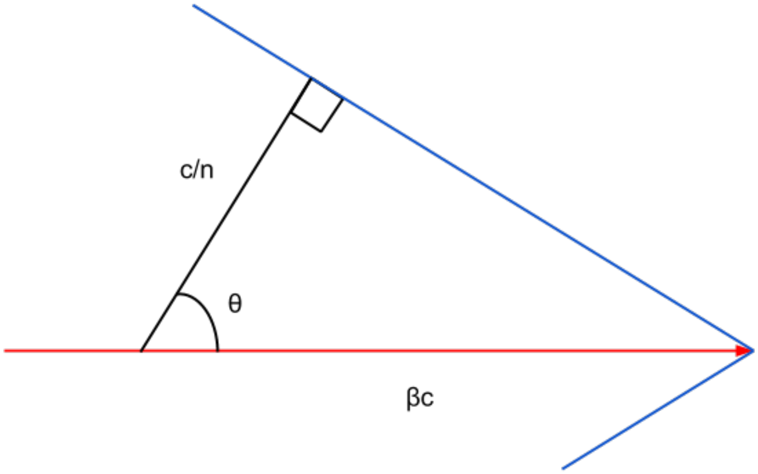

Figure 3.3: A particle traveling at βc emits photons at a speed of c/n, creating a particular angle between the particle and resulting Cherenkov radiation.

$$E_{th} = \frac{nmc^2}{\sqrt{n^2 - 1}} \tag{3.3}$$

The spectrum of Cherenkov radiation is defined by the Frank-Tamm equation, shown in Eq. 3.4.

$$\frac{\partial^2 N}{\partial x \partial \lambda} = \frac{2\pi\alpha}{\lambda^2}(1 - \frac{1}{\beta^2 n(\lambda)^2}) \tag{3.4}$$

The number of photons emitted is inversely proportional to the wavelength squared, which indicates that the spectrum peaks in the lower wavelengths that are still above threshold. For most materials, this is in the blue or UV range. This is shown for the material used by the BHM detector in Fig. 3.4.

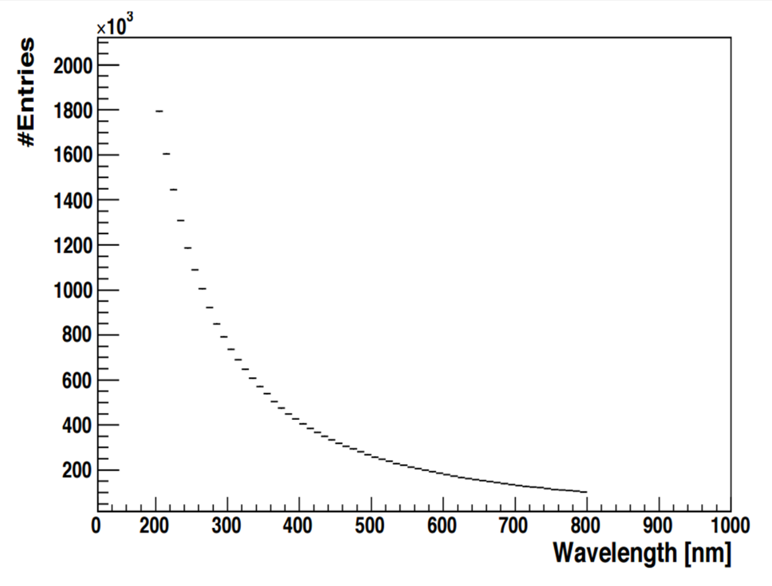

Figure 3.4: The spectrum of Cherenkov radiation created in quartz.

The Cherenkov medium used in the BHM detectors is fused silica, which has an index of refraction of $n \simeq 1.46$ in the UV [16]. For muons, a main contributor to the MIB rate, this value is 140MeV. Based on simulations, nearly all muons in the beam halo are expected to be above this threshold, as shown in Fig. 3.5 [1].

3.2 Directionality

The base of a BHM detector unit is a fused silica cylinder optically coupled to a photomultiplier tube (PMT). The detector units are oriented in such a way that when a MIB

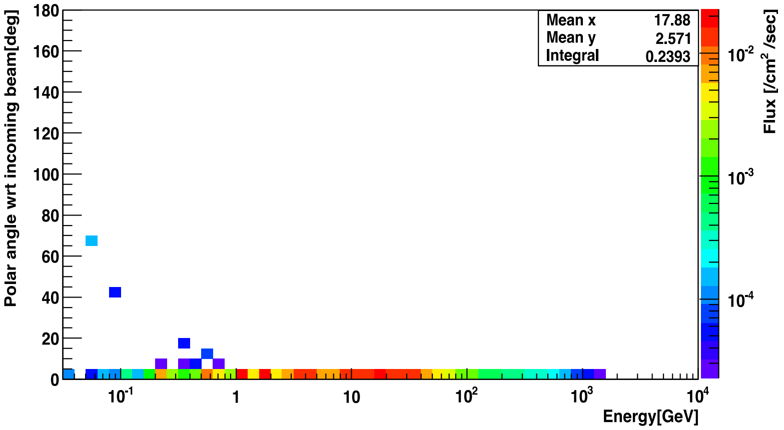

Figure 3.5: Most muons in the beam halo have energies around 10GeV, much higher than the threshold energy of 140MeV.

muon arrives with the incoming beam and produces Cherenkov radiation in the quartz, the light propagates forward and is collected by the PMT. On the other hand, collision (PP) products arrive in the opposite direction. While they still produce Cherenkov radiation, the resulting photons propagate in the opposite direction and are absorbed by black paint that is applied to the other end of the cylinder. Both of these processes are shown in Fig. 3.6.

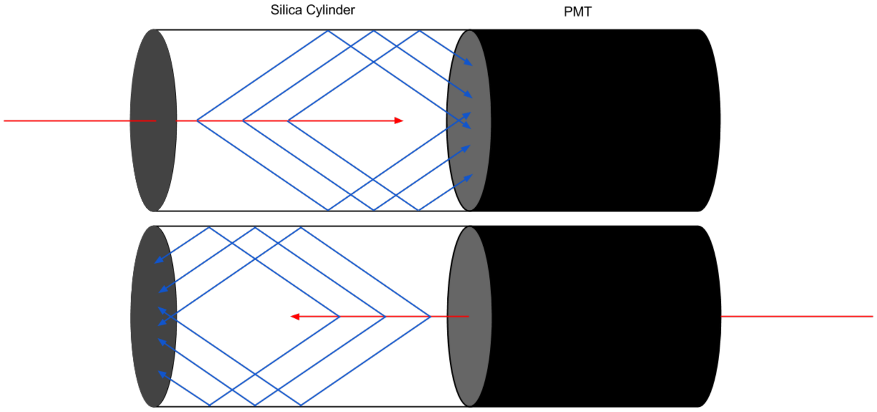

Figure 3.6: *Top:* A MIB muon arrives with the incoming beam and produces Cherenkov radiation, which is detected by the PMT. *Bottom:* A PP product arrives in the opposite direction, and the Cherenkov radiation that is produced is absorbed by black paint at the end of the cylinder.

Consequently, signals from forward particles are larger than from backward particles. Even signals from other isotropic background sources, such as cosmic rays, are, on average, small, relative to MIB signals. This concept was tested with particle beams at CERN in 2012 [1], and DESY in 2014 [17]. A PMT waveform for both a forward and backward particle is shown in Fig. 3.7.

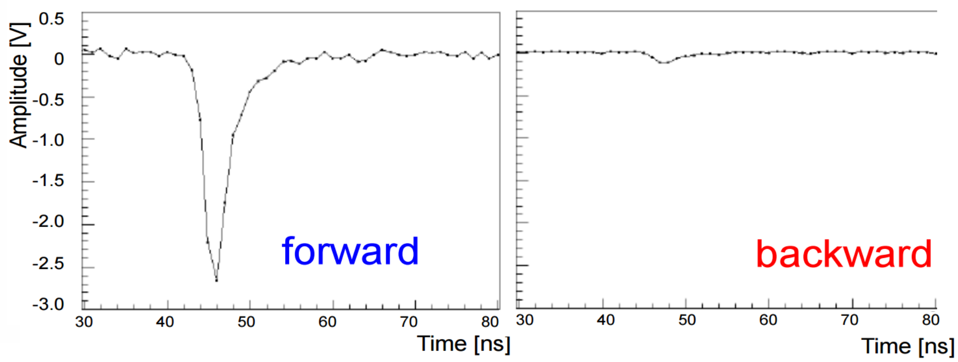

Figure 3.7: *Left:* PMT waveform from a forward particle in the 2012 CERN test beam. *Bottom:* PMT waveform from a backward particle in the 2012 CERN test beam.

It was further demonstrated that by implementing a charge amplitude cut on all signals, it is possible to suppress signals from backward particles by a factor of 10^4 while maintaining an efficiency close to 100% for MIB signals [17], as shown in Fig. 3.8.

3.3 Timing

In addition to using the directional nature of the MIB and PP particles, the BHM detector uses precise timing to separate these two types of events.

Since the bunches from the LHC collide in CMS at the interaction point every 25ns, and all products are traveling with the beams at the velocity of light, it is possible to select a location along the beam line, called a *golden location*, where the time difference (δt) between the arrival of MIB and PP particles is maximized. These locations are shown in Figure 3.9.

The BHM detectors were placed at one of these locations on each side of CMS in order to take advantage of this property. Even when the separation in timing is maximized, good time resolution is required in order to separate the two types of events.

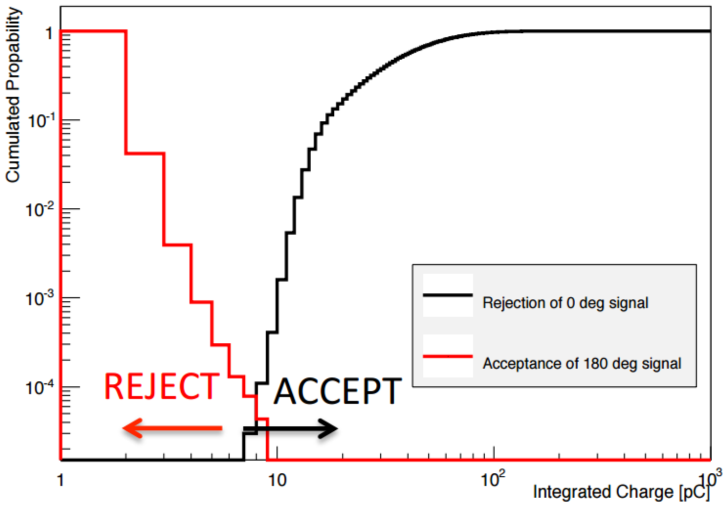

Figure 3.8: Cumulative integral of the normalized distributions of the signal charge measured for electrons with angles of 0° and 180°.

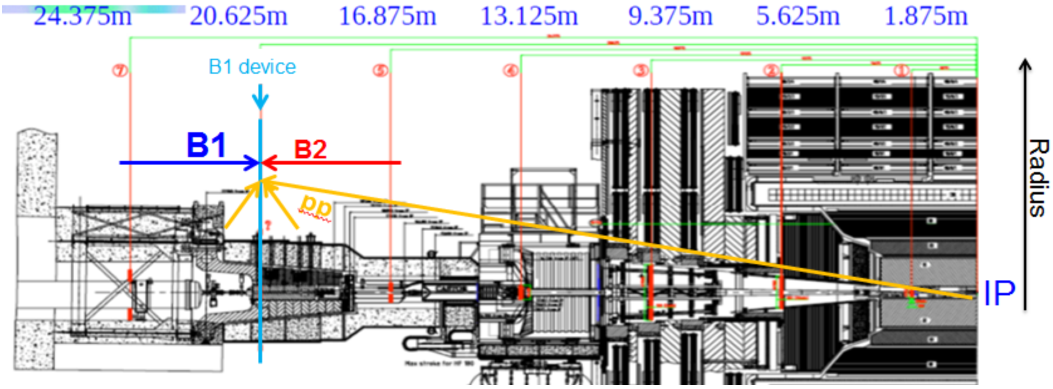

Figure 3.9: Golden locations near CMS.

Chapter 4

Implementation and Installation

An overview of the BHM systems, as installed, will be presented. The installation of the detector units occurred in February and March of 2015. Installation of the electronics for the detector continued through July 2015. Commissioning of the full system is ongoing at the time of writing. The author made significant contributions to all parts of this process, but especially in the testing of detector units, installation and cabling of the system, the testing of electronics, and data-taking and analysis of initial results from commissioning.

4.1 Geometry

The BHM detector consists of 40 individual detector units installed at golden location 6, which is 20.625m from the interaction point. This golden location is on the rotating shielding, which is on both ends of CMS, outside the bulk of the experiment.

The main motivation for selecting this site was the result of simulations performed to assess the flux of particles at various locations. Golden location 6 was shown to have a relatively high flux of MIB particles when compared to PP products. This location was chosen for a number of additional reasons, including the lack of obstructions caused by any other detectors or services, the small residual magnetic field from the CMS solenoid, the relatively low radiation dose, and the relatively easy access for cabling.

The units are arranged around the rotating shielding at a radius of 1.8m from the beam pipe. Aluminum structures attached to either side of the magnetic shielding hold

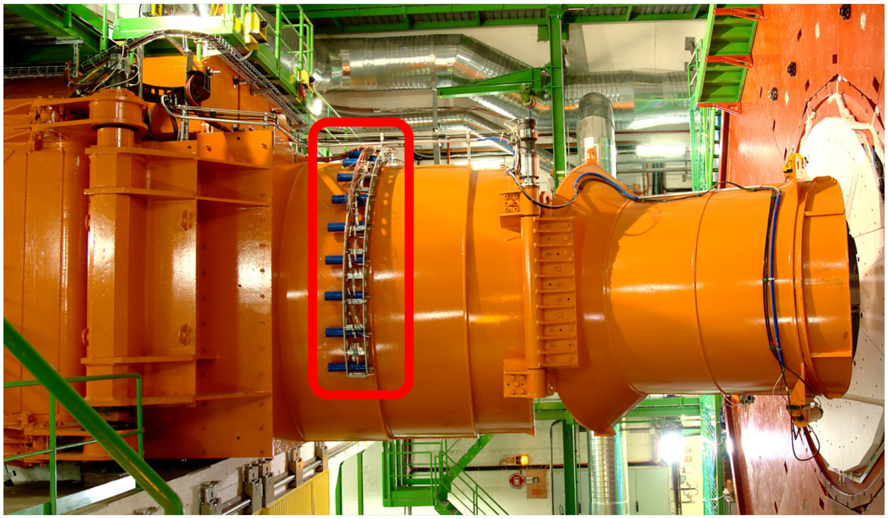

Figure 4.1: Location of the BHM detector on the magnetic shielding.

ten units each, amounting to twenty units on each end. The units on each end measure the background rate for the incoming beam. Each side on each end is referred to as a quadrant. They are distinguished by being at the +Z or -Z end of CMS and on the NEAR or FAR side of the cavern.

The detector units are evenly distributed, beginning at a ϕ value of $-30°$ and continuing through 210°, as shown in Fig. 4.2.

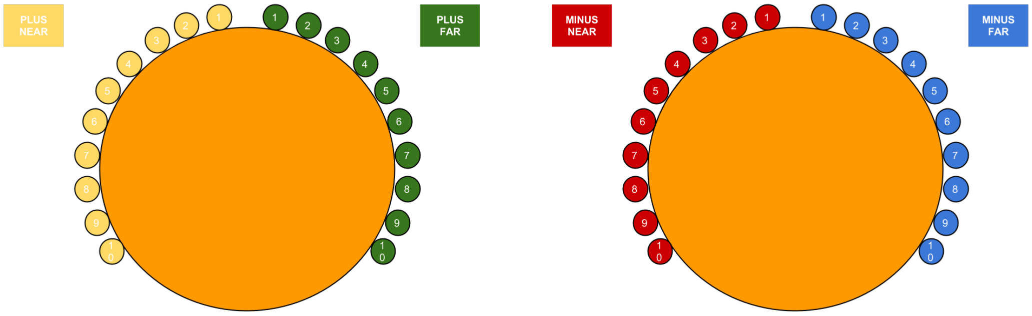

(a) +Z distribution

(b) -Z distribution

Figure 4.2: Distribution of BHM detector units.

The bottom third of the rotating shielding is not covered because, as can be seen in Fig. 4.3, this region experiences the lowest flux. This is due to absorption of MIB particles by the floor of the LHC tunnel.

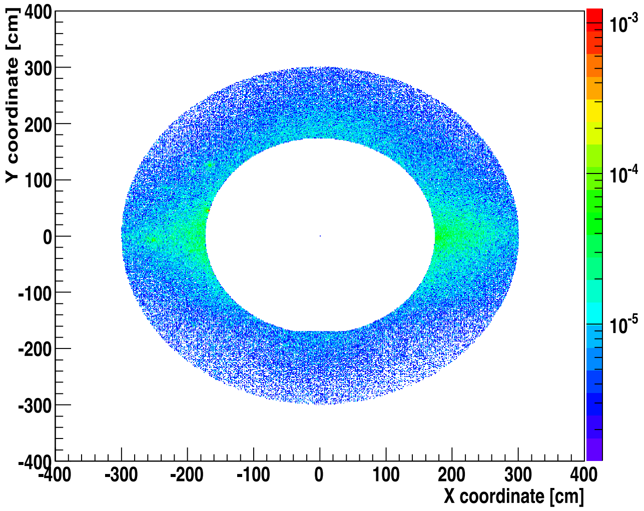

Figure 4.3: ϕ distribution of normalized flux of MIB particles [1].

4.2 Detector Units

The Cherenkov medium used in the detector units is a 10cm cylinder of SQ0 synthetic fused silica [16], which is 5.2cm in diameter. The cylinder is attached to a UV-sensitive PMT of the same diameter. A silicon disk is interposed to optimize the optical coupling. The other end of the cylinder is painted black in order to absorb the Cherenkov radiation that propagates in the opposite direction. The basic components of a unit can be seen in Fig. 4.4.

The PMT chosen for the detectors is the R2059 model manufactured by Hamamatsu [18]. It was selected for its UV-sensitivity and size. The plot of quantum efficiency versus wavelength can be seen in Fig. 4.5. A large size and flat window was desirable in order to cover a large cross section and still match the silica cylinder in diameter.

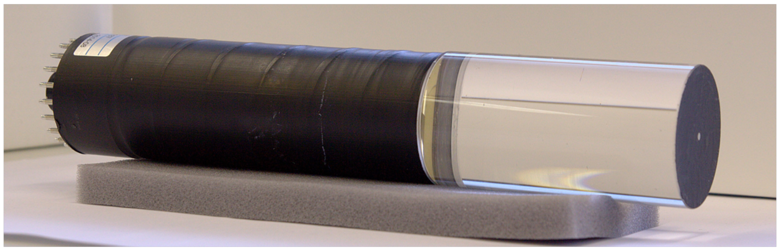

Figure 4.4: The base of a BHM detector unit - a quartz bar coupled to a PMT.

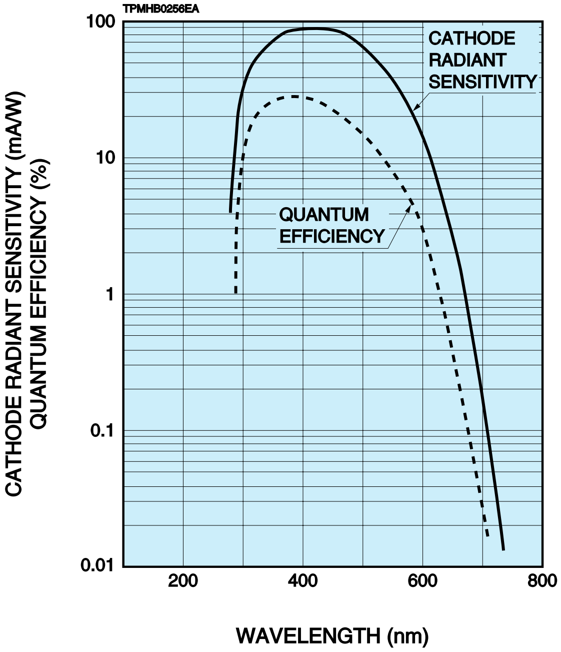

Figure 4.5: Quantum efficiency versus wavelength for the R2059 PMT.

A significant disadvantage is that this PMT is very sensitive to magnetic fields owing to its traditional dynode construction. Still, it was the best compromise between sensitivity, price, and availability.

Before the detector units were assembled, the dark count rate of the PMTs was measured in order to find a stable operating voltage for each PMT. The relative gain between all units was also found [17].

After the units had been assembled, the author was responsible for testing them for light transmission efficiency. This process is discussed in more detail in Section 4.3.

4.2.1 Shielding

In order to protect the sensitive PMT from the magnetic field, three layers of magnetic shielding were used in the detector units.

The first is a layer of Permalloy [19], as shown in Fig. 4.6(a). In addition to shielding, it serves as the mechanical support for the PMT and quartz bar. It is firmly attached to the base of the PMT using screws and ensures that the PMT does not separate from the silica cylinder.

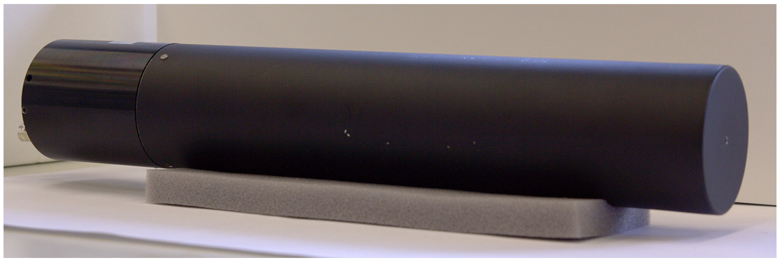

(a) Permalloy layer

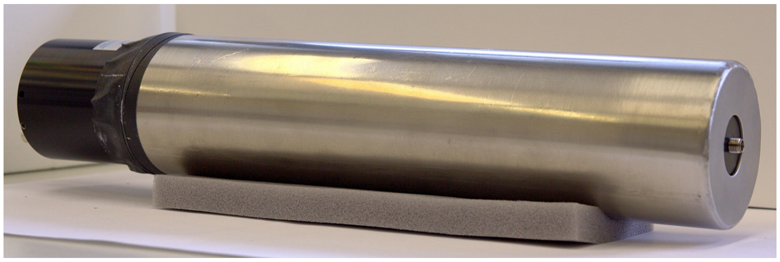

(b) Mumetal layer

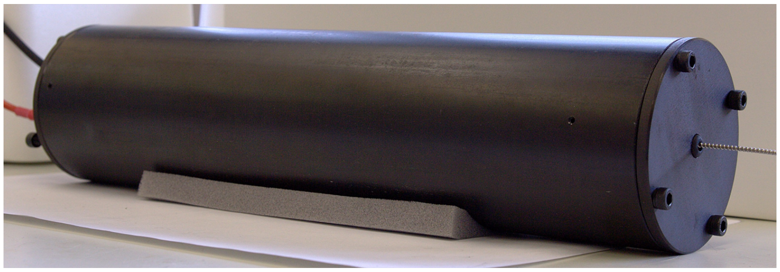

(c) Outer layer

Figure 4.6: Three layers of magnetic shielding for the BHM detector units.

The second is a layer of mu-metal [20], as shown in Fig. 4.6(b). It is separated from the first layer by thick, plastic spacers. The first two layers have very high permeability but saturate at very low field values.

A 1cm thick cylinder of iron is used as the third and final layer. It was selected because, while it has a lower permeability, it does not saturate at the magnetic fields that will be experienced by the detector units. This layer also absorbs the large flux of low-energy particles present in the cavern. It is again separated from the second layer with plastic spacers. The unit is closed by iron caps at both ends. The cap near the base of the PMT has two holes - one for a signal cable and one for the high voltage (HV) cable. The other end has a single hole for the insertion of an optical fiber from the calibration system.

The efficiency of the magnetic shielding was tested with the calibration system as the magnetic field in the CMS solenoid was activated, and reductions in the PMT response were seen. These are seen in Fig. 4.7(a).

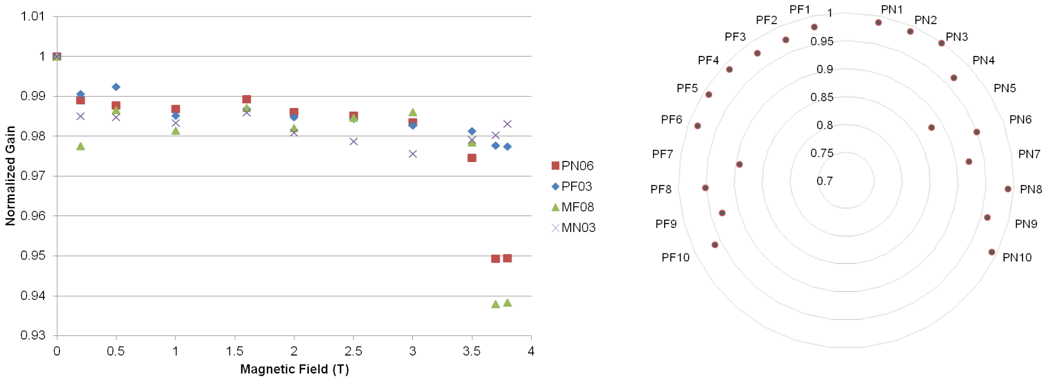

(a) PMT gain vs. Magnetic field

(b) % decrease in PMT gain at 3.8 T

Figure 4.7: *Top:* Normalized PMT gain versus magnetic field strength, shown for four sample units. *Bottom:* Percentage decrease in PMT gain at maximum field of 3.8T, shown for all units measuring beam 1.

Figure 4.7(b) shows the percentage decrease for units measuring one beam, when the CMS solenoid is at full field. The units around the horizontal plane experienced a larger decrease than those at the top, because the residual magnetic field is stronger in the central areas. The largest decrease observed was on the order of 10%. This drop will not affect the detection efficiency, as the signal is large, and both the signal and background will be reduced in amplitude. The author worked with another University of Minnesota student to perform this analysis.

Once the detector units had been installed in the CMS cavern, a final test was performed to ensure that the shielding was light-tight. Pedestal data was taken while the lights in the CMS cavern remained on, and was taken again after the lights had been turned off. The ratio of the two results was taken, and no significant difference was seen. The result for a single detector unit is shown in Fig. 4.8.

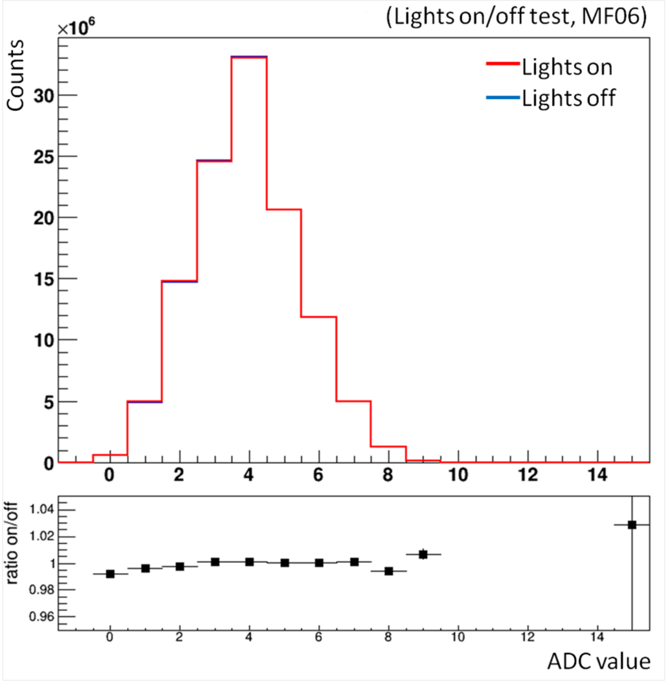

Figure 4.8: Detector units showed no change in response, regardless of light in the CMS cavern.

The author was responsible for performing this test and analyzing the resulting data.

4.3 Calibration System

A calibration system [17] was installed in order to assess the detector performance over time as radiation damage and aging effects start to become significant. It is also useful for commissioning the system. The calibration system is designed to distribute light pulses of known amplitude to all detector units in order to measure variation in PMT response. An overview of the final system can be seen in Fig. 4.9.

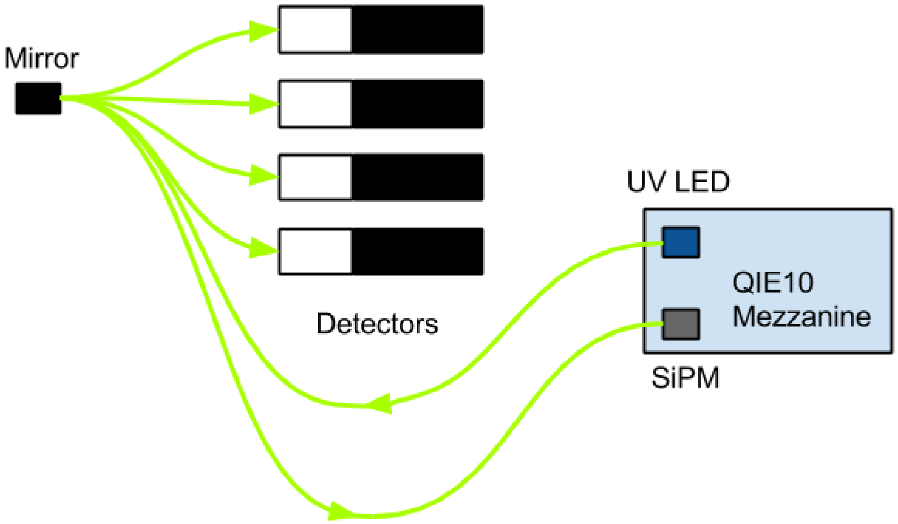

Figure 4.9: Overview of the calibration system.

Each quarter receives a signal from a UV light emitting diode (LED), which is distributed to all units, as well as a reference silicon photomultiplier (SiPM), via quartz optical fibers [21]. The references serve to compensate for any variation based on fluctuations of the LED itself.

The transmission fibers are attached to the detector units through a small hole in the shielding where the light enters the silica cylinder through a small hole in the black paint. The signal is divided by a splitter with 12 fibers attached to a mirror, as shown in Fig. 4.10. One of the 12 fibers acts as the source, while 11 copies of the signal are reflected back to the ten detector units and one reference SiPM.

Before the units and calibration system were installed, two different tests were performed. The set-up for both is shown in Fig. 4.11.

First, the detector units were tested for transmission efficiency of light pulses from the calibration system. A blue LED, driven by a pulse generator, was attached to one fiber of the optical splitter used in the calibration system. One PMT, which was never changed, was attached to another fiber to serve as a reference. The PMT being

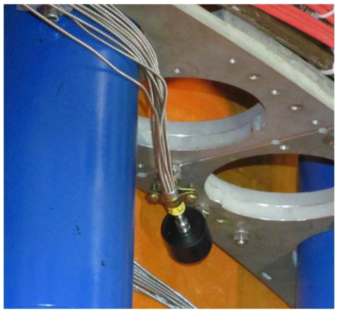

Figure 4.10: The optical splitter, made of 12 optical fibers attached to a mirror.

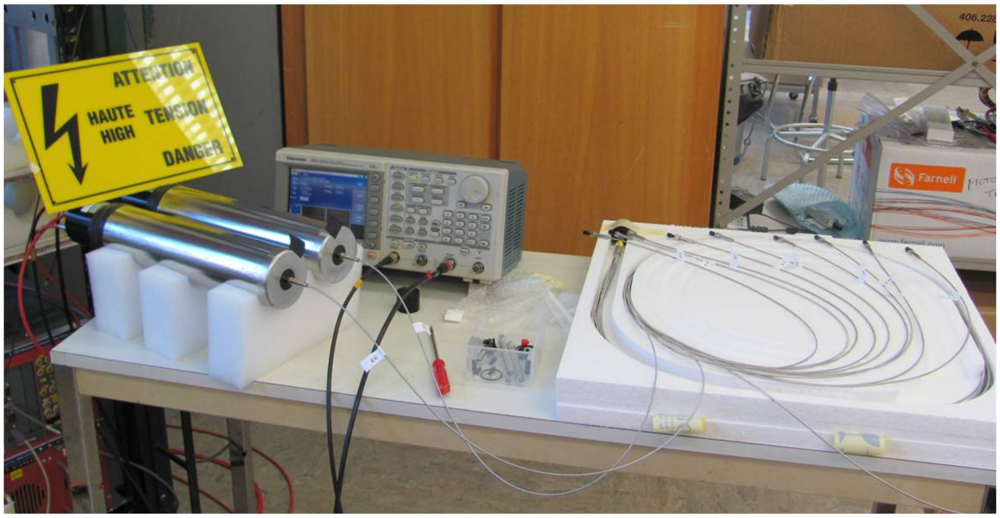

Figure 4.11: Set-up for the tests performed on detector units and calibration system.

tested was attached to a third fiber. The signal from both PMTs was read out by an oscilloscope.

The alignment of the hole in the black paint, holes in the shielding, and fiber within its housing is very precise, and some units are more aligned than others. This caused variation in response of the PMT as the fiber was rotated, since the asymmetry affected how much light reached the quartz cylinder. For this reason, the fiber attached to the PMT being tested was rotated until a maximum signal amplitude was found. Once this maximum was located, it was possible to fix the fiber in this position, and maintain a constant signal. This test was performed for all detector units after the second layer of shielding had been added and again after the final layer had been added.

The second test characterized individual fibers of the calibration system and was performed in a very similar manner. One detector unit was connected to each fiber of the calibration system, and the signal was recorded.

These tests served as a quality control for units before they were installed. Indeed, it was found that some of the units had to be sent back and remade. At the end of the testing period, all units were approved for installation.

Also based on these two tests, it was determined which fibers and which detector units had the highest light transmission efficiency. In order to make system response more homogeneous when the calibration system is in use, symmetric units were paired with asymmetric fibers, and vice versa.

4.4 Electronics

In order to discriminate signals and measure a background rate of MIB particles, the electronics of the BHM detector requires sensitivity to amplitude, sub-bunch crossing timing resolution, and an absence of dead time. One system that meets all these requirements is the μTCA-based system that has been developed for the CMS HCAL upgrade [22]. A schematic of the system, as implemented for BHM, is shown in Fig. 4.12.

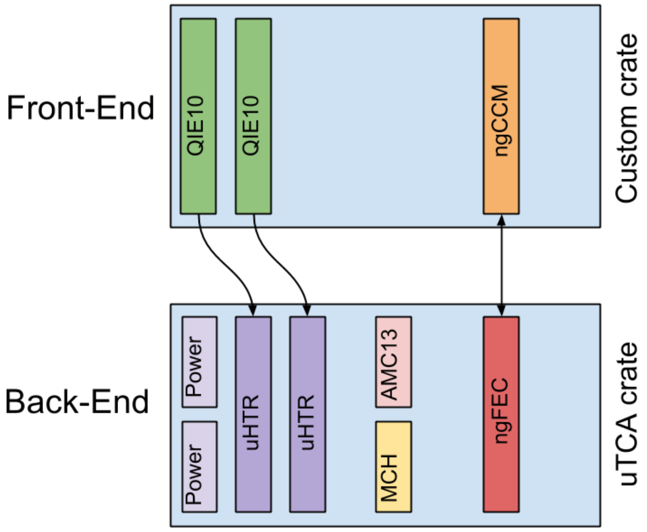

Figure 4.12: An overview of the BHM electronics.

4.4.1 Front-End Electronics

The analog signals coming from the PMTs are fed into a patch panel, shown in Fig. 4.13. In addition to splitting the signal, the patch panel also serves as an attenuator, because the largest signals would otherwise exceed the input range of the front-end card. From there, the signals are then sent to the BHM electronics.

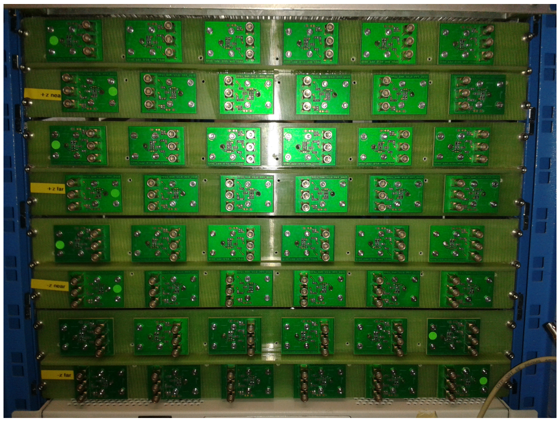

Figure 4.13: An image of the patch panel.

The front-end electronics crate shares the mechanical form factor of a standard VME [23] crate, including dimensions and connectors, but has a custom backplane. There are lines for power, clock, and slow controls, which are driven by a Next Generation Clock Control Module (ngCCM) [22].

The main front-end board serves to acquire the analog signals from the detector PMTs and digitize them. An image of the board can be seen in Fig. 4.14.

The main component of the board is a set of 24 charge integrating Application Specific Integrated Circuits (ASICs) called the Charge Integrator and Encoder version 10 (QIE10) [24]. Each ASIC can handle one channel, so two boards are needed to accommodate all 40 detector channels. The QIEs integrate the signal over 25ns and produce an 8-bit amplitude, or ADC, number. The chip has a non-linear, dynamic scale for the amplitude with a range of 0-339pC. It also produces a 6-bit timing, or TDC value. This value is between 0 and 49 and corresponds to the 0.5ns interval when the leading edge of the signal passes a certain threshold. In this way, it covers the whole 25ns bunch crossing.

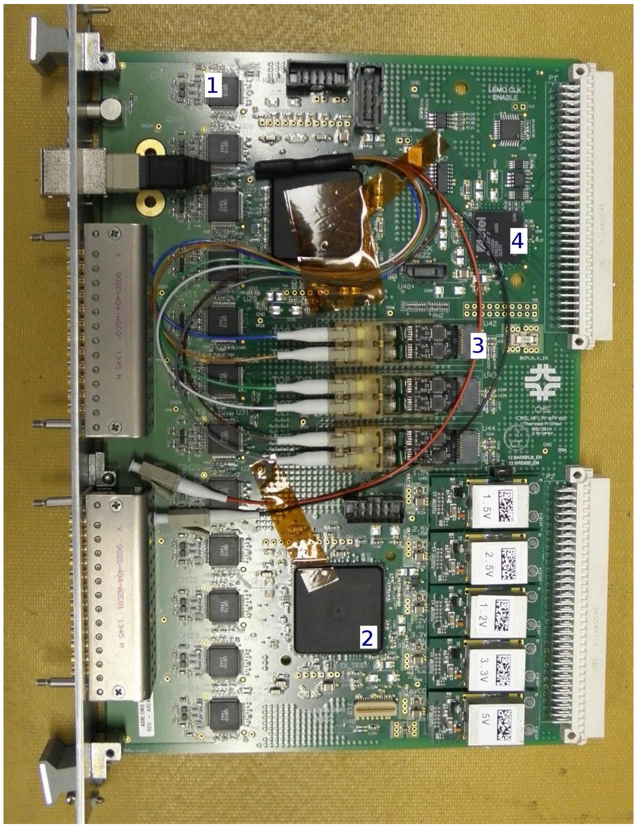

Figure 4.14: An image of the QIE10 board.

Once the data has been digitized, it is read out and formatted by two Igloo2 Field Programmable Gate Arrays (FPGAs) for transmission via a 5Gbps optical link to the back-end. These FPGAs also provide the capability to adjust the clock phase for individual QIE channels, which will be used to adjust the timing to compensate for different cable delays in each channel. The final component of the board is a bridge FPGA, which is responsible for control and monitoring. The implementation of this front-end board in the BHM electronics will serve as the first demonstration in CMS of the QIE10 and 5Gbps asynchronous optical link between front-end and back-end electronics.

Additionally, a mezzanine card will be attached to the QIE10 board in the final system. It will power and control four UV LEDs for the calibration system, one for each quarter of the detector. The reference SiPMs will also be mounted directly on the mezzanine.

4.4.2 Back-End Electronics

The back-end electronics uses the μTCA standard [25]. Within the μTCA crate, there are slots for up to twelve Advanced Mezzanine Cards (AMCs) and two slots for 'housekeeping' modules.

The main data-processing card for the back-end is called the μTCA HCAL Trigger and Readout, or μHTR [26], and sits in an AMC slot of the μTCA crate. Two of them are used in the BHM system. Twenty four of the μHTR channels are used, so that one μHTR is matched to each QIE10 board.

The μHTR makes uses of two main FPGAs. Data is received via a 5Gbps optical link by the first FPGA. A selection is applied based on the individual channel amplitude thresholds that are set in the hardware by the user. This feature is crucial because it can be used to mask PMT noise, cosmic events, and PP products. During commissioning, the author was responsible for setting the amplitude thresholds. Low amplitudes were typically used for commissioning purposes. These were set by taking data while there was no beam in the LHC and by determining a rough cut-off value in the amplitude of the cosmic events. While these thresholds did not exclude MIB signals, they also did not exclude a substantial fraction of the PP signals.

In the same FPGA, the TDC value is mapped to one of four TDC bins for each event. The time intervals within a single bunch to which these bins are mapped can be selected with a 500ps resolution. The bins serve to group hits that arrive at similar times. For example, one bin could be set to the time range when MIB events are expected, the next set to the range when PP events are expected, and the last two set for any late or early hits. In this way, it is possible to distinguish MIB and PP events based on the timing of the signals, with a minimum load on the data flow.

The second FPGA is dedicated to creating per-channel occupancy histograms. Events passing the amplitude threshold are binned by their location in the orbit. Since there are 3654 bunch positions in a orbit and 4 TDC bins per bunch, there are 14256 bins per histogram. Each histogram is integrated for 2^{14} orbits, or about 1.5 seconds. With regular beam conditions, based on the MIB rate, one would expect order of 20 events/histogram. For this reason, only nine bits are reserved for each bin.

Along with applying the amplitude cuts and mapping the TDC values, the first FPGA is responsible for creating a per-channel set of 1D amplitude histograms. These histograms have 256×4 bins - four for each possible ADC value. Within each ADC value, the events are further split based on TDC bin. These histograms were used solely for commissioning and calibration purposes.

The firmware for both FPGAs was tested by the author. A script was written to generate 'data' in the format required by the μHTR. Then, MiniCTR2 [27] was used to feed that data into the μHTR. A back-end communication tool, called μHTRtool, was used to look at the resulting histograms and to ensure that the data was read-out as expected.

In addition to the μHTRs, several specialty cards are required in the back-end crate. A MicroTCA Carrier Hub (MCH) [22] card must sit in one of the designated housekeeping slots. This card is responsible for a variety of control functions, including distribution of power and read out of data via ethernet link.

A special AMC, called an AMC13 [28], also sits in one of the housekeeping slots. It is used to aggregate data, as well as to distribute timing information from the Trigger Control and Distribution System (TCDS), which carries the global LHC clock. In addition, a Next Generation Front End Control Card (ngFEC) occupies one of the twelve AMC slots [22]. This card receives TCDS fast commands from the AMC13 and slow control commands via ethernet from the software. It merges these two information streams into a link, at 4.8Gbps, which is received by the ngCCM. The ngCCM then splits the incoming stream into its fundamental components and distributes them on the backplane using a dedicated line.

4.4.3 VME System

A VME system was installed to serve as a back-up while the QIE10 system is being commissioned. It is fed by the second copy of the PMT signal from a divider on the patch panel.

The VME system has two separate functions, so the signal is split again as it enters the system. One signal copy is used to produce a background rate with no extra timing information, and the other is used to make an amplitude measurement of the incoming signals. An overview of the system is shown in Fig. 4.15.

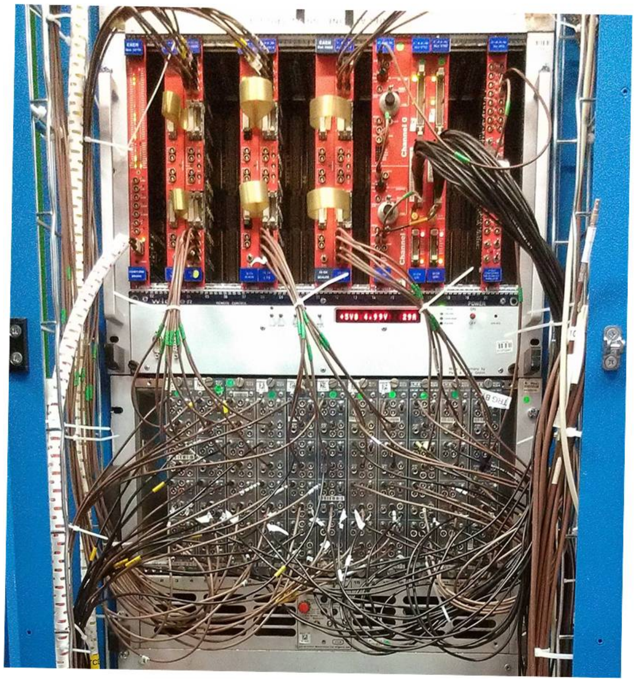

Figure 4.15: The VME system.

4.5 Software

Once the histograms have been filled in the uHTRs, they are read out through the MCH by the BHM software. The software is written using the BrilDAQ framework, which was developed for use by all BRIL subdetectors. It is based on the xDAQ framework [29], which is common to much of the CMS data acquisition system. In BrilDAQ, there is a main eventing bus through which data can be transmitted. Software applications can then act as publishers when they write data to this bus and subscribers when they read data from this bus. The whole process, as implemented in BHM, can be seen in Fig. 4.16.

The main BHM publisher reads histograms from the μTCA electronics and publishes them to the BHM eventing bus. There is also an option to store the unprocessed raw data. The main BHM subscriber, which is a separate application, then subscribes to the histograms on BHM eventing and uses them to calculate a MIB rate. The MIB rate is then published to the main BRIL eventing bus. From there, it is published to CMS

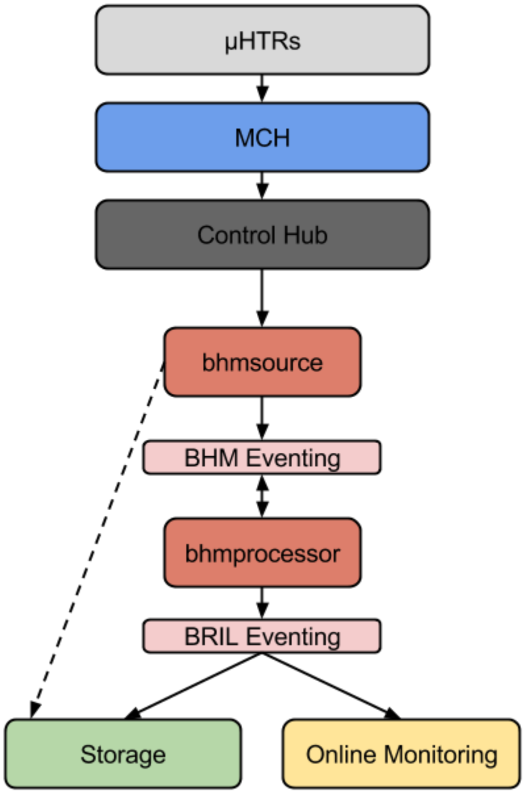

Figure 4.16: Data flow diagram for the BHM software.

and the LHC approximately every 23s. It is also sent to storage for offline analysis.

Chapter 5

Detector Commissioning

The BHM detector entered the commissioning phase with the advent of first beams of Run II. First results are presented here.

Throughout commissioning and until the introduction of functional BHM software, the author operated the electronics, wrote data-taking scripts for all tests performed, and carried out the data collection.

5.1 Splashes

Beam splashes are special beam events in which the LHC operators direct a single bunch of protons directly into the tertiary collimators, which are located immediately before the experimental cavern. This sends a spray of secondary particles into the cavern and through the experiment. All the particles are traveling in the same direction at the speed of light, and thus arrive at the same time. A splash event in CMS is shown in Fig. 5.1.

These events are used by the most of the CMS detector components for calibration. They are particularly useful for BHM, owing to the purely directional nature of each event. The expected response from BHM consists of large signals in the units measuring the background rate for the beam for which the splash event is happening, followed by smaller signals in the units measuring the other beam. Since the BHM detector sits at golden location 6, the expected time between the two signals is the equivalent of 5.5 bunch crossings, or 137.5ns. When taking into account the physical geometry of the

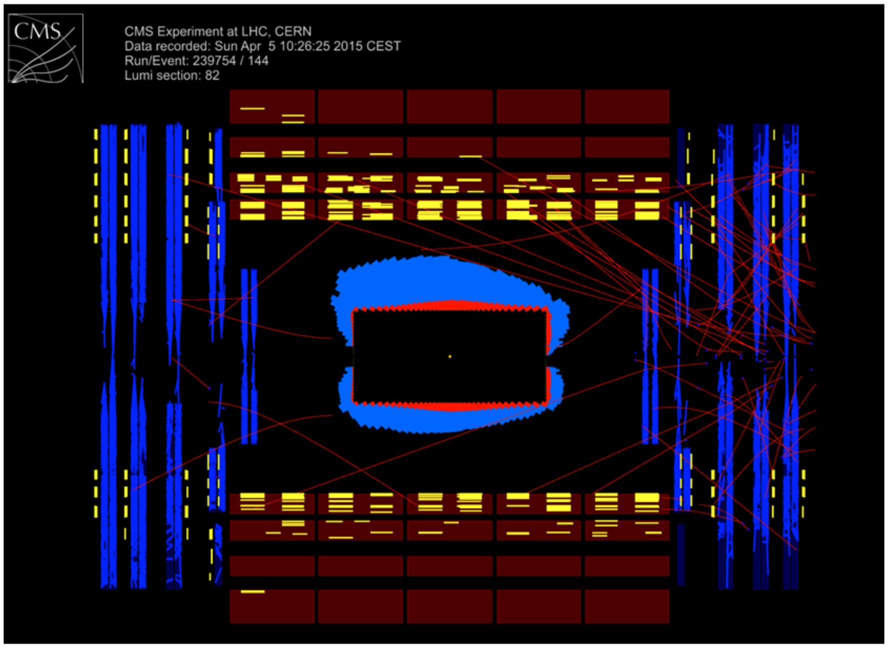

Figure 5.1: A splash event seen in CMS.

detector units, this difference is reduced to 135ns.

The first splash events of Run II took place on April 7, 2015. Approximately 20 splashes per beam were recorded. A sample event, collected with an oscilloscope connected directly to the output of two detector units, is shown in Fig. 5.2. The initial, large signal in a beam 2 detector unit, followed by the smaller signal in a beam 1 detector unit, can be seen. The time delay observed is approximately 135ns. This served as a first indication that the BHM detector units were functioning as expected.

The occupancy histograms collected over the splash events are shown in Fig 5.3. The data shown is for two units, one measuring for beam 1 and one measuring for beam 2, during beam 2 splashes. The first spike is the forward signal. The second spike, seen in the opposite unit, is the backward signal. At the time of the splashes, the system only had a timing resolution of a whole bunch crossing, but it is still clear that the backward signal comes six bunch crossings after the forward signal, as is expected.

Amplitude data for these events was taken as well. The graph given in Fig. 5.4 shows the splash event amplitudes for both beams from a single unit that was measuring the background for beam 2. During beam 2 splashes, there were numerous high-amplitude

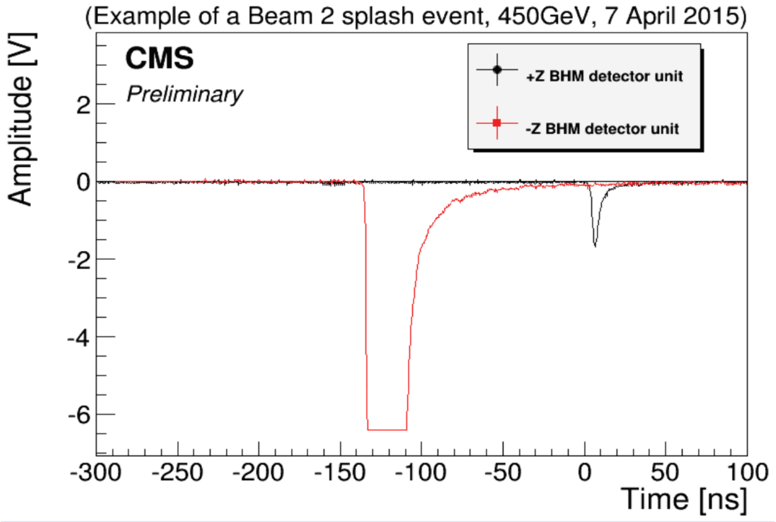

Figure 5.2: A PMT signal from both a beam 1 and beam 2 detector unit during a beam 2 splash event.

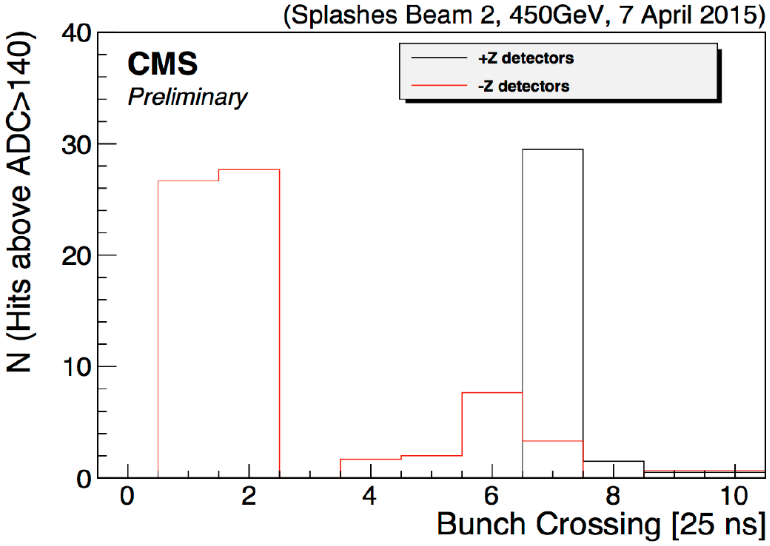

Figure 5.3: Occupancy histograms from both a beam 1 and beam 2 detector unit during a beam 2 splash event.

events seen. Comparing the signal seen during beam 1 splashes to that seen during a no beam period, no distinct difference is seen. This indicated that while the unit saw many high-amplitude forward particles, no high-amplitude backward particles were observed.

This served as the first indication of the directional sensitivity of the BHM detectors.

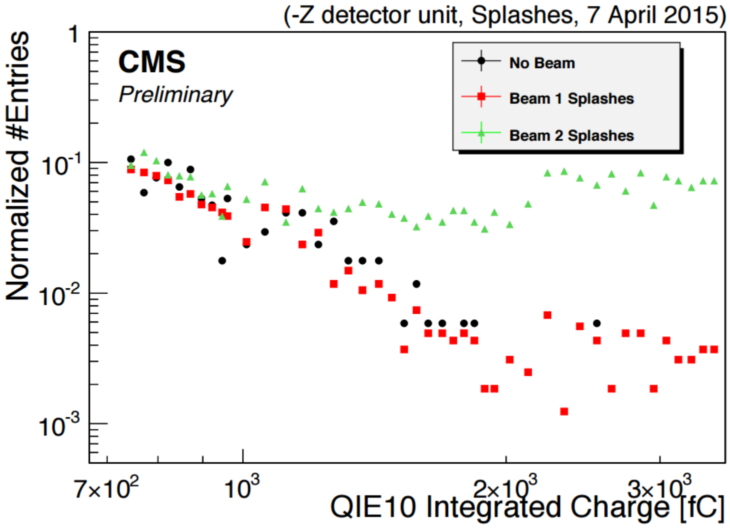

Figure 5.4: Amplitude data from a beam 2 detector for beam 1 splashes, beam 2 splashes, and no beam.

At the time of this test, the final BHM software had not been completed. In order to take data, a back-end communication tool called uHTRtool was used. The author was responsible for operating the uHTR through the use of this tool, as well as performing the analysis of the data.

5.2 Correlation to Collimator Operation

In a collimator scan, the jaws of the collimator are moved in until they begin to intercept the beam, and are then returned to their open state. These scans are expected to be a large source of MIB particles. A set of collimator scans was captured by the VME system. The data collected during the scan are shown in Fig. 5.5.

When the collimator gap decreases, as shown by the dotted lines, the background rate is seen to increase. A large spike is observed when the collimator gap is reduced to approximately 7mm. The background then decreases as the collimators are moved back out. The trend is similar for both beams. This served as additional evidence that the BHM system is sensitive to the desired background.

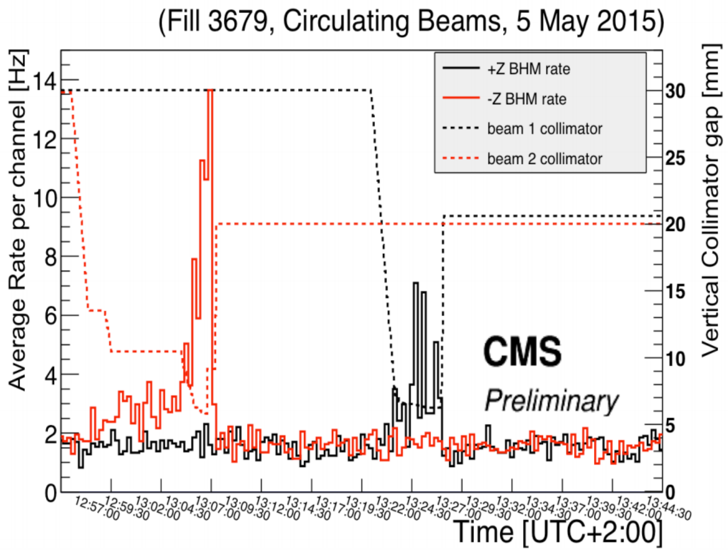

Figure 5.5: MIB rate, as measured by the VME system, correlates to the collimator gap.

5.3 Collisions

Data from stable collisions were collected with low signal amplitude thresholds. An LHC fill (fill 3858) was chosen for its relatively simple bunch structure. There were six bunch trains, each with six bunches spaced at 50ns. There were also several single bunches. The detailed bunch structure can be seen very clearly in the occupancy histogram, as shown in Fig. 5.6. The spikes are the bunch trains. These are followed by a tail of hits, of which the timing is consistent with the expected lifetime of particles in the CMS cavern.

A closer look at one of the bunch trains reveals more details, as can be seen in Fig. 5.7. The first three filled bins, in yellow, are purely MIB halo particles. The first collision products are seen approximately 22 TDC bins, or 5.5 bunch crossings, later, as expected. This pattern then continues for six subsequent bunches.

The first detail to note is that all MIB events end up in a single bin - always TDC bin 1. This demonstrates that they are all coming in the same 6.25ns window within every bunch. Alternatively, the particles from collisions come mainly in different TDC bins - either 0 or 3. This means that BHM will be able to successfully distinguish MIB

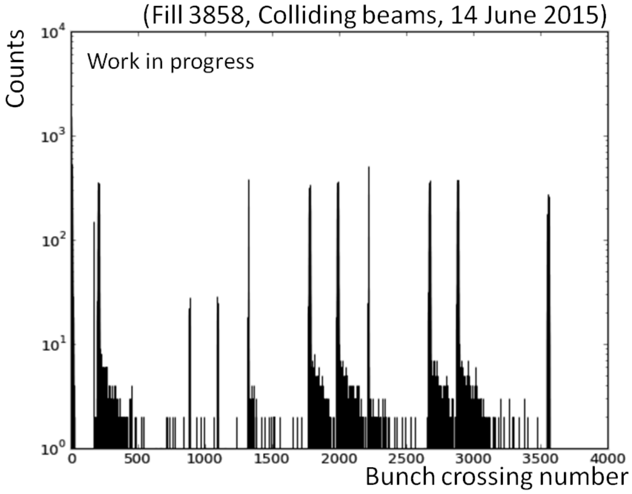

Figure 5.6: Summed occupancy histograms for fill 3858 from a single detector unit.

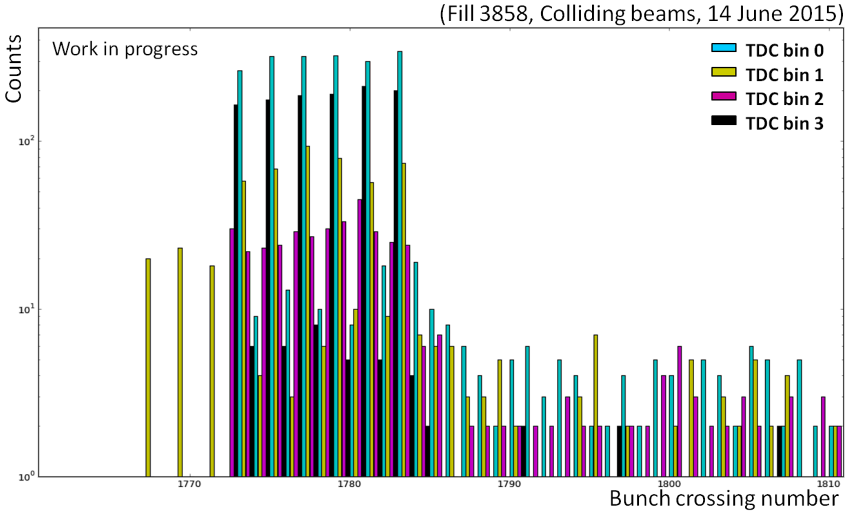

Figure 5.7: A closer look at a bunch train in fill 3858 from a single detector unit.

and PP particles based on the sub-bunch crossing timing information coming in the form of TDC bin.

Chapter 6

Summary

The new BHM detector will provide an online, bunch-by-bunch, per beam MIB rate arriving at CMS at high radius. It is composed of 40 individual detector units located 20.6 m from the interaction point and arranged around the beams at a radius of 1.8 m. The base of each unit is a fused silica cylinder optically coupled to a UV-sensitive PMT. This design takes advantage of the directional nature of Cherenkov radiation and golden location timing to separate MIB particles from PP products.

Every bunch crossing, the analog signals from the PMTs are sent to the front-end and are digitized by QIE10 ASICs. They are sent to the back-end via 5 Gbps asynchronous optical link, which serves as the first demonstration of this type of link. In the back-end, μHTRs apply an amplitude threshold, map the signals to four TDC bins, and create occupancy histograms. MIB rates are calculated in software and published to CMS and the LHC.

The whole detector was successfully installed in CMS during LS1. Preliminary results show that the detector is sensitive to MIB particles produced through interactions with collimators. The directional aspect of the detector units was seen during splash events, meaning that amplitude can be used to distinguish MIB particles and PP products. These signals can be further differentiated through the use of sub-bunch crossing timing, as seen during stable collisions.

Moving forward, there is more work to be done in order to fully commission the new detector, which will be performed as the LHC operation improves. Final front-end, back-end, and calibration electronics must be installed, tested, and integrated into the system. Slow control commands will be incorporated into the software framework to allow for more robust monitoring and control of the front-end electronics. Thresholds will need to be adjusted and set based on future collision data. Final edits to the software must be made in order to improve efficiency and usability, and complete background rate calculation algorithms must be implemented. Lastly, detailed background studies will be performed and compared with simulation.

References

[1] S. Orfanelli et al. Design of a novel Cherenkov detector system for Machine Induced Background monitoring in the CMS cavern. In *Proceedings of IBIC2013*, Oxford, UK, 2013.

[2] L. Evans and P. Bryant. LHC machine. *JINST*, 3(08), 2008.

[3] S. Chatrchyan et al. The CMS experiment at the CERN LHC. *JINST*, 3, 2008.

[4] The ATLAS Collaboration. The ATLAS Experiment at the CERN LHC. *JINST*, 3(08), 2008.

[5] S. Chatrchyan et al. Observation of a new boson with mass near 125 GeV in pp collisions at $\sqrt{s} = 7$ and 8 TeV. *JHEP*, 1306, 2013.

[6] G. Aad et al. Observation of a new particle in the search for the Standard Model Higgs boson with the ATLAS detector at the LHC. *Phys.Lett.*, B716, 2012.

[7] A. Dabrowski. Upgrade of the CMS instrumentation for luminosity and machine induced background measurements. Technical Report CMS-CR-2014-362, CERN, Geneva, Oct 2014.

[8] J. L. Leonard et al. Fast Beam Condition Monitor for CMS: performance and upgrade. *Nucl. Instr. and Meth. A*, 765, 2014.

[9] M. Guthoff. *Radiation Damage to the diamond-based Beam Condition Monitor of the CMS Detector at the LHC*. PhD thesis, CERN, 2014.

[10] S. Muller. *The Beam Condition Monitor 2 and the Radiation Environment of the CMS Detector at the LHC*. PhD thesis, Karlsruhe U., Karlsruhe, 2011.

[11] R. W. Assmann et al. Equilibrium Beam Distribution and Halo in the LHC. (LHC-Project-Report-592.), Jul 2002.

[12] O. S. Bruning et al. *LHC Design Report.* CERN, Geneva, 2004.

[13] *The CMS muon project: Technical Design Report.* Number 97-032. CERN, Geneva.

[14] P. Čerenkov. Visible radiation produced by electrons moving in a medium with velocities exceeding that of light. *Phys. Rev.*, 52, Aug 1937.

[15] C. Mead. Quantum theory of the refractive index. *Phys. Rev.*, 110, Apr 1958.

[16] J-Plasma. SQ sinthetic quartz. URL: `www.j-fiber.com/en/18/download/1542/130930122442_DB-KAP-001-00-0111-j-SQ-Q0-Q1-QT-subgrades.pdf`.

[17] Nicolo Tosi. *The new Beam Halo Monitor for the CMS experiment at the LHC.* PhD thesis, Alma Mater Studiorum Università di Bologna, 2015.

[18] Hamamatsu Photonics K.K. R2059 Photomultiplier Tube. URL: `www.hamamatsu.com/us/en/R2059.html`.

[19] G.W. Elmen and Arnold H.D. Permalloy, a new magnetic material of very high permeability. *Bell System Tech. J.*, 2, Jul 1923.

[20] J.G. Henry and S.S. Willoughby. Magnetic alloy, 1926. US Patent 1,582,353.

[21] Ceramoptec. Ceramoptec optran fibers. URL: `www.ceramoptec.com/pure-silica-core-fiber.php`.

[22] *CMS Technical Design Report for the Phase 1 Upgrade of the Hadron Calorimeter.* Number 2012-015. CERN, Geneva.

[23] VITA. *VME64 Standard.* Number S2011. 1994.

[24] A. Baumbaugh et al. QIE10: a new front-end custom integrated circuit for high-rate experiments. *JINST*, 9(01), 2014.

[25] PICMG. *Micro Telecommunications Computing Architecture.* Number MTCA.0 R1.0. 2006.

[26] Mans J. M. HCAL uHTR Specifications and Operational Documentation. URL: `cms-docdb.cern.ch/cgi-bin/PublicDocDB/ShowDocument?docid=12306`.

[27] J Mans and E Frahm. Status report on a microtca card for hcal trigger and readout at slhc. *Journal of Instrumentation*, 5(12):C12027, 2010. URL: `http://stacks.iop.org/1748-0221/5/i=12/a=C12027`.

[28] E. Hazen et al. The AMC13XG: a new generation clock/timing/DAQ module for CMS MicroTCA. *JINST*, 8(12), 2013.

[29] V. Brigljevic et al. Using XDAQ in application scenarios of the CMS experiment. *FERMILAB-CONF-03-293, CHEP-2003-MOGT008*, 2003.

Appendix A

Acronyms

Care has been taken in this thesis to minimize the use of jargon and acronyms, but this cannot always be achieved. This appendix contains a table of acronyms and their meaning.

A.1 Acronyms

Table A.1: Acronyms

Acronym	Meaning
ADC	Analog-to-Digital Converter
AMC	Advanced Mezzanine Card
ASIC	Application Specific Integrated Circuit
BHM	Beam Halo Monitor
BRIL	Beam, Radiation, Instrumentation, and Luminosity
CERN	European Organization for Nuclear Research
CMS	Compact Muon Solenoid
DIP	Data Interchange Protocol
ECAL	Electromagnetic Calorimeter
FPGA	Field-Programmable Gate Array

Continued on next page

Table A.1 – continued from previous page

Acronym	Meaning
HCAL	Hadron Calorimeter
HF	Forward Hadron Calorimeter
HV	High Voltage
LED	Light Emitting Diode
LHC	Large Hadron Collider
LS1	Long Shutdown 1
MCH	MicroTCA Carrier Hub
MIB	Machine-induced Background
ngCCM	Next Generation Clock Control Module
ngFEC	Next Generation Front-end Control
NIM	Nuclear Instrumentation Module
PMT	Photomultiplier Tube
QDC	Charge-to-Digital Converter
QIE	Charge Integrator and Encoder
SiPM	Silicon Photomultiplier
TCDS	Trigger, Control, and Distribution System
TCP	Target Collimator Primary
TCS	Target Collimator Secondary
TCT	Target Collimator Tertiary
TDC	Time-to-Digital Converter
μHTR	MicroTCA HCAL Trigger and Readout
VME	Versa Module Europa
VTTX	Versatile Twin-Transmitter